

Image formation in CARS microscopy: effect of the Gouy phase shift

K. I. Popov,^{1,*} A. F. Pegoraro,^{2,3} A. Stolow,^{2,3} and L. Ramunno¹

¹Department of Physics, University of Ottawa, Ottawa, Ontario K1N 6N5, Canada

²Steele Institute for Molecular Sciences, National Research Council of Canada, Ottawa, Ontario, K1A 0R6, Canada

³Department of Physics, Queen's University, Kingston, Ontario, K7L 3N6, Canada

[*kpopov@uottawa.ca](mailto:kpopov@uottawa.ca)

Abstract: Image formation in Coherent Anti-Stokes Raman Scattering (CARS) microscopy of sub-wavelength objects is investigated via a combined experimental, numerical and theoretical study. We consider a resonant spherical object in the presence of a nonresonant background, using tightly focused laser pulses. When the object is translated along the laser propagation axis, we find the CARS signal to be asymmetric about the laser focal plane. When the object is located before the focus, there is a distinct shadow within the image, whereas the brightest signal is obtained when the object is behind the focus. This behaviour is caused by interference between resonant and nonresonant signals, and the Gouy phase shift is responsible for the observed asymmetry within the image.

© 2011 Optical Society of America

OCIS codes: (170.1650) Coherence imaging; (180.4315) Nonlinear microscopy; (170.5660) Raman spectroscopy.

References and links

1. A. Zumbusch, G. R. Holtom, and X. S. Xie, "Three-Dimensional Vibrational Imaging by Coherent Anti-Stokes Raman Scattering," *Phys. Rev. Lett* **82**, 4142–4145 (1999).
2. J.-X. Cheng and X. S. Xie, "Coherent Anti-Stokes Raman Scattering: Instrumentation, Theory, and Applications," *J. Phys. Chem. B* **108**, 827–840 (2004).
3. C. Evans and X. S. Xie, "Coherent Anti-Stokes Raman Scattering Microscopy: Chemical Imaging for Biology and Medicine," *Annu. Rev. Anal. Chem.* **1**, 883–909 (2008).
4. E. O. Potma and X. S. Xie, "Theory of Spontaneous and Coherent Raman scattering," in *Handbook of Biological Nonlinear Optical Microscopy*, B. R. Masters and P. T. C. So, eds. (Oxford University Press, 2008), pp. 164–185.
5. M. D. Duncan, J. Reintjes, and T. J. Manuccia, "Scanning coherent anti-Stokes Raman microscope," *Opt. Lett.* **7**, 350–352 (1982).
6. C. L. Evans, E. O. Potma, M. Puoris'haag, D. Côté, C. P. Lin, and X. S. Xie, "Chemical imaging of tissue in vivo with video-rate coherent anti-Stokes Raman scattering microscopy," *Proc. Natl. Acad. Sci. USA* **102**, 16807–16812 (2005).
7. A. F. Pegoraro, A. Ridsdale, D. J. Moffatt, Y. Jia, J. P. Pezacki, and A. Stolow, "Optimally chirped multimodal CARS microscopy based on a single Ti:sapphire oscillator," *Opt. Express* **17**, 2984–2996 (2009).
8. M. Rivard, M. Laliberté, A. Bertrand-Grenier, C. Harnagea, C. P. Pfeffer, M. Vallières, Y. St-Pierre, A. Pignolet, M. A. El Khakani, and F. Légaré, "The structural origin of second harmonic generation in fascia," *Biomed. Opt. Express* **2**, 26–36 (2011).
9. J.-X. Cheng, A. Volkmer, and X. S. Xie, "Theoretical and experimental characterisation of coherent anti-Stokes Raman scattering microscopy," *J. Opt. Soc. Am. B* **19**, 1363–1375 (2002).
10. A. D. Slepov, A. Ridsdale, A. F. Pegoraro, D. J. Moffatt, and A. Stolow, "Multimodal CARS microscopy of structured carbohydrate biopolymers," *Biomed. Opt. Express* **1**, 1347–1357 (2010).
11. A. Taflove and S. C. Hagness, *Computational Electrodynamics*, 3rd ed. (Artech House, 2005), pp. 58–79.

12. M. Fujii, M. Tahara, I. Sakagami, W. Freude, and P. Russer, "High-Order FDTD and Auxiliary Differential Equation Formulation of Optical Pulse Propagation in 2-D Kerr and Raman Nonlinear Dispersive Media," *IEEE J. Quantum Electron.* **40**, 175–182 (2004).
 13. K. I. Popov, C. McElcheran, K. Briggs, S. Mack, and L. Ramunno, "Morphology of femtosecond laser modification of bulk dielectrics," *Opt. Express* **19**, 271–282 (2011).
 14. A. Taflove and S. C. Hagness, *Computational Electrodynamics*, 3rd ed. (Artech House, 2005), pp. 186–212.
 15. G. Mur, "Absorbing Boundary Conditions for the Finite-Difference Approximation of the Time-Domain Electromagnetic-Field Equations," *IEEE Trans. Electromagn. Compat.* **EMC-23**, 377–382 (1981).
 16. A. Taflove and S. C. Hagness, *Computational Electrodynamics*, 3rd ed. (Artech House, 2005), pp. 329–343.
 17. R. W. Boyd, *Nonlinear Optics*, 2nd ed. (Academic Press, 2003), p. 194.
-

1. Introduction

Coherent Anti-Stokes Raman Scattering (CARS) is a parametric nonlinear optical process which underlies an increasingly important method for molecule-specific, non-invasive imaging of biological tissues and cells [1]–[4]. CARS has grown from first proof-of-principle experiments [5] to the high-performance facilities capable of obtaining high-resolution CARS images with video frequency [6]. Combined with other nonlinear imaging modalities, CARS microscopy has become a promising tool for *in-vivo* real-time studies of biological processes [7].

A correct interpretation of the images formed via parametric nonlinear microscopies such as CARS, however, requires detailed consideration of the image formation process. In fluorescence microscopy, the macroscopic response of the ensemble of molecules within the laser focus is the incoherent sum of all the microscopic (per molecule) responses. As such, the relationship between the spatial distribution of signal intensity and the spatial distribution of molecules generating the signal is one-to-one. In parametric nonlinear optical microscopy, this is not the case because the macroscopic response is the coherent sum of the microscopic responses and depends therefore on the local order (symmetry, alignment etc.) of signal generating molecules within the focal volume. For example, signals from molecules within different spatial regions of the laser focal volume can destructively interfere with each other, greatly altering the image and, therefore, its interpretation. Parametric nonlinear microscopy of sub-wavelength structures may introduce distortions into the image that cannot always be predicted by models. For example, recent microscopy experiments using another parametric process, second harmonic generation (SHG), showed that image formation was not simply related to the concentration of the species being probed [8]. Similar distortions were previously discussed for backward direction-detected CARS signals [9].

It is our aim to investigate the nonlinear optical image formation process in samples that are spatially heterogeneous on sub-wavelength scales. Here we present the first results of a combined numerical-experimental program designed to investigate the details of nonlinear image formation in CARS microscopy. We begin with the images of the simplest of systems, a spherical polystyrene bead embedded in a featureless substrate, in order to clearly demonstrate effects of the coherent, parametric nature of CARS microscopy. We find, somewhat counter-intuitively, that the detected CARS signal is asymmetric with respect to the bead's physical location along the laser propagation axis. Our experiments reveal that the maximum anti-Stokes image intensity appears when the bead is located behind the laser focus. By contrast, when the bead is located before the laser focus, a 'shadow' appears in the image, *i.e.*, the signal decreases below the level of the nonresonant background. Although a very simple system, this shadow formation and the apparent displacement and asymmetry of the bead indicates the need for a clear understanding of the image formation process.

The paper is organized as follows. In Section 2 we present experimental observations of an asymmetric intensity pattern detected from a small polystyrene bead translated along the laser axis. Section 3 provides a description of detailed FDTD calculations, which show that the effect

occurs only for a resonant scatterer in the presence of a nonresonant background. An analytical model of asymmetric pattern formation is developed in Section 4, where the role of the Gouy phase shift in the shadow formation is determined.

2. Experimental observations

The experimental setup utilized here has been previously described elsewhere [10]. Briefly, a femtosecond Ti:Sapphire oscillator output is split, with part of the beam used to pump a photonic crystal fiber (PCF) and the other used as the pump beam. The continuum from the PCF is filtered, then chirped using a block of SF6 glass and used as the Stokes pulse. The Stokes beam is recombined with the remainder of the Ti:Sapphire light. The combined beams are sent to an Olympus Fluoview FV300 confocal laser scanning microscope modified for multiphoton microscopy. A minor change compared to previous work is that the 10 cm block of SF6 was removed for the experiments described here. To ensure that the Stokes and pump beam were overlapped in space, gold nanoparticles were dried onto a coverslip and imaged. The best focus position was independently measured for the pump and Stokes and found to be identical within measurement error.

The sample used was 1 μm polystyrene fluorescent beads (Polysciences Inc.) suspended in an agarose gel. The two-photon excited fluorescence (TPEF) due to the pump was collected in the epi-direction. CARS was tuned to the resonance of the polystyrene beads ($\sim 2850\text{ cm}^{-1}$) and was collected in the forward direction. The axial response of several beads were averaged. The location of each bead with respect to the best laser focus was determined by the TPEF signal, which is maximal for a bead at the best focus. The displacement of the bead relative to the focus was generated by moving the objective lens. The axial response as a function of the displacement from the focal point of the pump is shown in Fig. 1a, demonstrating that the peak of the CARS response is displaced from the peak of the TPEF. Furthermore, there is a clear decrease in the CARS signal for beads located on the other side of the focus.

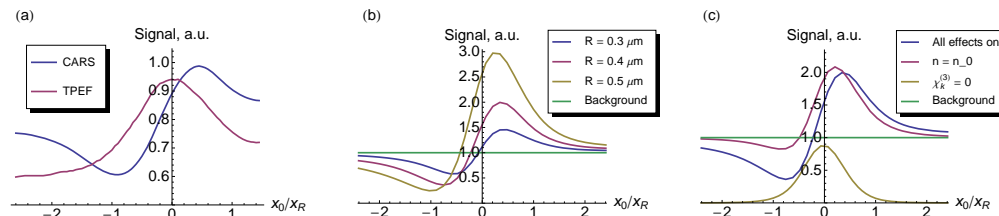


Fig. 1. (Color online). (a) Measured axial response of suspended polystyrene beads as a function of normalized displacement from the laser focus. The TPEF signal maximum is taken as the optimal focal position. The CARS signal is measured on resonance at $\sim 2850\text{ cm}^{-1}$. (b) Far-field integrated CARS signal vs. scatterer position relative to the best focus as calculated via FDTD, for scatterers of varying radius R , and for no scatterer. (c) FDTD calculated CARS signal for $R = 0.4\ \mu\text{m}$ as in (b), including the cases where the background is index matched, and the background has no nonresonant nonlinear response. x_0 is the position of the bead, x_R is the Rayleigh length of the laser beam focusing lens ($\sim 4\ \mu\text{m}$ in experiment, $\sim 2\ \mu\text{m}$ in simulations) at the pump frequency.

This phenomenon can lead to appearance of artefacts in CARS microscopy images. Fig. 2 shows images of polystyrene beads embedded in agarose gel for two different axial focal positions. In Fig 2a, the laser is focused at a depth of $12.8\ \mu\text{m}$ into the sample. The arrows indicate some dark spots (shadows) that are clearly visible in the image. In Fig 2b the focus

position is moved to a depth of $8.8 \mu\text{m}$, *i.e.*, closer to the laser source. The shadows of Fig 2a, have now turned into bright spots in Fig 2b.

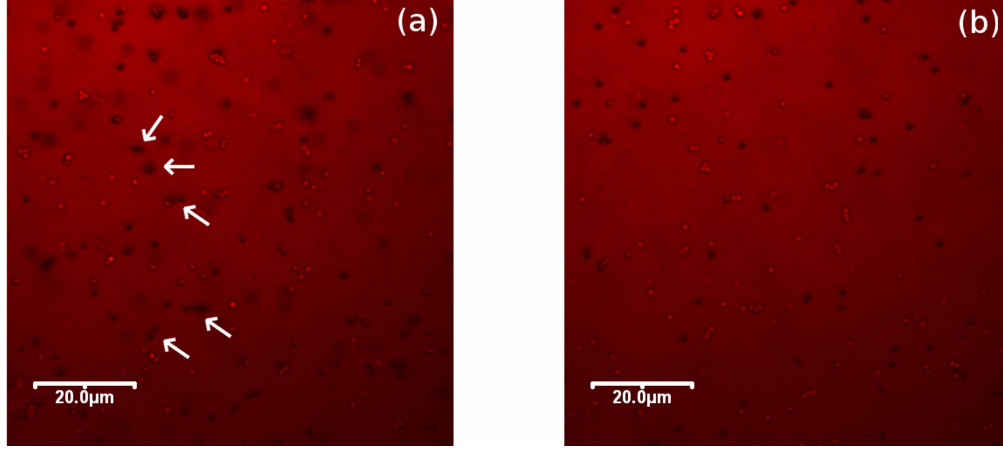


Fig. 2. CARS images of $1 \mu\text{m}$ diameter polystyrene beads embedded in agarose gel taken (a) $12.8 \mu\text{m}$ and (b) $8.8 \mu\text{m}$ deep into the sample. The CARS images were taken at a Raman shift of 2850 cm^{-1} . The arrows show examples of dark spot artefacts in image (a), which correspond to bright spots in image (b).

3. Numerical simulations

To understand the experimental CARS signal in Fig. 1a, we developed a numerical tool that simulates the near-field interaction between the tightly focused laser sources and a small scatterer, as well as performs the far field detection. For the near-field interaction, we solve the 3D Maxwell equations in CGS units, $\nabla \times \vec{E} = -(1/c)\partial\vec{B}/\partial t$, $\nabla \times \vec{H} = (1/c)\partial\vec{D}/\partial t$, using the Finite-Difference-Time-Domain (FDTD) method [11] with the constitutive relations

$$\begin{aligned}\vec{D} &= [1 + 4\pi(\chi^{(1)}(\vec{r}) + \chi_k^{(3)}(\vec{r})E^2)]\vec{E} + 4\pi\vec{P}_R, \\ \vec{H} &= \vec{B},\end{aligned}\quad (1)$$

where $\chi^{(1)}$ and $\chi_k^{(3)}$ are the first- and third-order instantaneous susceptibilities, respectively. The Raman polarization of the resonant medium \vec{P}_R is evaluated according to [12]

$$\vec{P}_R(\vec{r}, t) = \frac{1}{4\pi}\vec{E} \cdot (\chi_R(\vec{r}, t) * E^2(t)). \quad (2)$$

where * symbol denotes a convolution integral and

$$\chi_R(\vec{r}, t) = \chi_R^{(3)}(\vec{r})\mathcal{F}^{-1}\left(\frac{\omega_R^2}{\omega_R^2 - \omega^2 + 2j\omega\gamma_R}\right). \quad (3)$$

In Eq. (3), $\chi_R^{(3)}(\vec{r})$ is the time-independent amplitude of the Raman susceptibility, ω_R the resonant frequency of molecular vibrations, and γ_R the damping factor; \mathcal{F}^{-1} denotes the inverse Fourier transformation. We use the auxiliary differential equation technique, described in detail in Ref. [12], for the numerical evaluation of Eq. (2).

To evaluate the field of the high-NA laser sources, broad Gaussian pulses of radius R_G , tightly focused by a high-NA paraboloidal mirror with radius $2.5R_G$, are calculated using a technique

described in a previous work [13]. For the on-axis case, which is what we consider here, a paraboloidal mirror is equivalent to a high NA objective lens that does not suffer from spherical aberrations. The field of the focused pulses is excited at the boundary of the simulation domain using the “Total-Field-Scattered-Field” technique [14]. The laser sources then propagate inside the domain, and are eventually absorbed at the opposite boundary by a first order Mur absorbing boundary condition [15]. The medium outside the FDTD simulation box is assumed to be linear and dispersionless. A near-to-far field transformation [16] in the frequency domain at the anti-Stokes frequency is used to generate the far-field signal, which is integrated over the solid angle subtended by the collecting lens to obtain the detected CARS signal (Fig. 3).

We take the pump wavelength to be 800 nm and the Stokes wavelength 1042 nm. The homogeneous background medium has refractive index $n_0 = 1.33$ and a Kerr nonlinearity with $\chi_k^{(3)} = 5.4 \times 10^{-14}$ esu [17], which is responsible for the nonresonant signal generation. A single Raman-active sphere of radius R and linear refractive index $n = 1.5$ was situated at various locations along the laser propagation axis \hat{x} . Both the pump and Stokes pulses have a Full-Width-at-Half-Maximum (FWHM) of 300 fs, and are focused by a paraboloidal mirror with NA = 1.1. The value of $\chi_R^{(3)}$ within the Raman-active sphere was chosen such that the resonant-to-nonresonant signal ratio, measured from interaction with a bulk medium, is equal to 50 [7]. A typical simulation was performed in a $12 \times 13 \times 13 \mu\text{m}^3$ box with 40^3 grid points per μm^3 . The scattered light was evaluated in the far field and integrated over a solid angle corresponding to a detector lens with NA = 0.6.

Figure 1b shows the magnitude of the detected integrated CARS signal as a function of position of the scatterer center along the laser axis, for scatterers of radius $R = 0.3, 0.4, 0.5 \mu\text{m}$. We find results similar to the experimental observations plotted in Fig. 1a: there is a distinct shadow in the image when the sphere is located before the laser focus. The calculated signal is also asymmetric, with the maximum occurring when the scatterer lies after the best focus.

To understand this pattern we re-ran the simulations for the $R = 0.4 \mu\text{m}$ scatterer, where we 1)

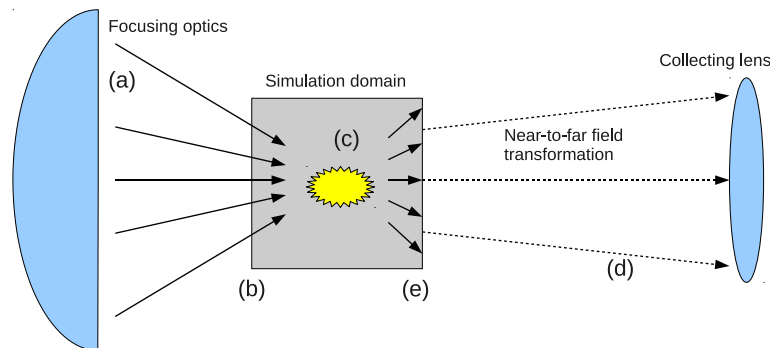


Fig. 3. The stages of the numerical experiment: (a) for each source pulse, a broad Gaussian beam is incident onto the surface of a high-NA paraboloidal perfectly reflecting macroscopic-sized mirror; (b) the electromagnetic field of the mirror is evaluated numerically at the boundary of the microscopic-sized simulation domain and is used as a boundary condition; (c) the laser pulses interact with the nonlinear media in the domain; (d) the scattered light is collected by the far-field probes and integrated over the appropriate solid angle; (e) the source pulses are absorbed by the absorbing boundaries of the simulation domain.

set the linear refractive index of the background equal to that of the scatterer by putting $n = n_0$, and 2) removed the nonlinear nonresonant background by putting $\chi_k^{(3)} = 0$. The resulting far-field integrated CARS signals are shown in Fig. 1c.

For case 1), where the linear refractive indices of the Raman-active scatterer and background material are equal, we find that the shadow is less dark, but does not disappear. The maximum signal of the bright spot appears somewhat brighter. This indicates that linear index mismatch is not the origin of the shadow and the maximum signal shift.

For case 2), where $\chi_k^{(3)} = 0$ and thus there is no generated nonresonant background signal, the detected CARS signal is completely symmetric around the best focus, with no evidence of a shadow. This indicates that the presence of the nonresonant background, and in particular, the interference between the nonresonant and resonant generated signals, has a profound effect on the actual detected CARS signal in the far field. We now discuss this interference in more detail.

4. Discussion

We begin by assuming that the laser fields can be approximately described by a Gaussian beam, and that the pump and Stokes fields (of frequencies ω_p and ω_s , respectively) have coinciding spot sizes w_0 and Rayleigh lengths $x_R = kw_0^2/2$, where k is the wave number (approximately equal for the pump and Stokes sources in this qualitative model). The propagation direction is \hat{x} and we take the laser focus to be the origin of our coordinate system. The resonant signal is generated by a Raman-active sphere located on the laser axis at $x = x_0$. Both the resonant signal amplitude and phase thus depend on x_0 . As we show in Appendix A, the forward-generated nonresonant and resonant signals in the continuous wave limit, as observed at the laser axis in the far-field zone at some point P , can be written as

$$\begin{aligned} E_{NR}(t) &= E_{0NR} \cos(\omega_{as}t + \phi_0), \\ E_R(x_0, t) &= \frac{E_{0R}}{[1 + (x_0/x_R)]^{3/2}} \cos(\omega_{as}t + \phi_0 + \pi/2 + \delta\phi_L + \phi_G(x_0)), \end{aligned} \quad (4)$$

where E_{0NR} is the amplitude of nonresonant signal, E_{0R} the amplitude of the resonant signal that would be generated by the sphere located at the origin, $\omega_{as} = 2\omega_p - \omega_s$ is the anti-Stokes frequency, ϕ_0 is an arbitrary phase constant that depends on the location of P , $\delta\phi_L$ is the linear phase shift originating from unequal refractive indices of the scatterer and background medium, and ϕ_G the Gouy phase shift. The latter depends on scatterer position, and is given by

$$\phi_G(x_0) = -\arctan(x_0/x_R). \quad (5)$$

Summing up the resonant and nonresonant fields in Eq. (4) one can readily obtain the intensity of the total signal

$$I \approx I_0 \left(1 + \frac{\rho^2}{[1 + (x_0/x_R)^2]^3} - 2 \frac{\rho \sin(\delta\phi_L + \phi_G)}{[1 + (x_0/x_R)^2]^{3/2}} \right), \quad (6)$$

where I_0 is the intensity of the nonresonant signal and $\rho = E_{0R}/E_{0NR}$. Eq. (6) is plotted in Fig. 4a. We estimated the linear phase shift by

$$\delta\phi_L \approx k(n - n_0)R, \quad (7)$$

which gives values of $\approx \pi/10, \pi/8, \pi/7$ for $R = 0.3, 0.4, 0.5 \mu\text{m}$, respectively. We have also set, correspondingly, $\rho = 0.4, 1, 2$ in Eq. (6), that is consistent with Fig. 1b. We find that the

shapes of our estimated signal in Fig. 4a match very well with our rigorously calculated signals in Fig. 1b. We thus conclude that Eq. (6) is a reasonable approximation and can be used for qualitative estimations.

When the phase shift $\delta\phi_L$ is set to zero (Fig. 4b), we find that the asymmetry in the signal remains, however with an increased maximum signal and a smaller depth of shadow. This is in qualitative agreement with our numerical results in Fig. 1c. On the other hand, when ϕ_G is set to zero (Fig. 4c), the patterns become symmetric, for both $\delta\phi_L = 0$ and $\delta\phi_L \neq 0$.

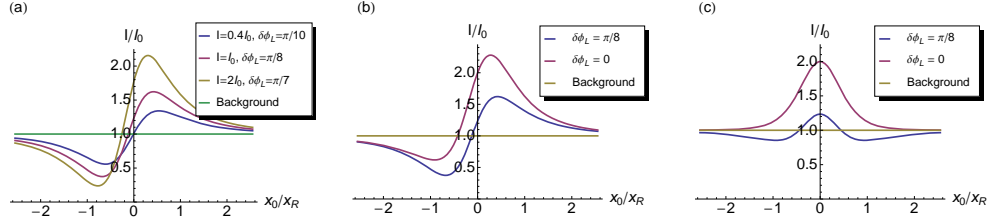


Fig. 4. (Color online). Intensity of the total far field signal as evaluated by Eq. (6) for $\rho = 0.4, 1, 2$ (a); for $\rho = 1$, $\delta\phi_L = \pi/8, 0$ and: $\phi_G \neq 0$ (b); and $\phi_G \equiv 0$ (c).

The dependence on x_0 enters Eq. (6) via the amplitude of the resonant signal and Gouy phase shift ϕ_G . The former is exactly symmetric about the laser focus ($x_0 = 0$) whereas the latter has different signs for $x_0 > 0$ and $x_0 < 0$. Therefore, it is the Gouy phase shift that is responsible for the asymmetry of the signal. While shadows do appear even if the Gouy phase shift is zero (cf. Fig. 4c, $\delta\phi_L = \pi/8$), albeit with a lower contrast, the maximum of the intensity shifts from the origin only if the Gouy phase shift is nonzero.

Finally, we note that if the nonresonant signal approaches zero ($\rho \rightarrow \infty$ and $I_0 \rightarrow 0$ in Eq.(6)), the dependence of the signal on the Gouy phase shifts disappears. It is thus important especially when the nonresonant and resonant signals are of comparable amplitude, which can occur for small Raman active scatters even in a weak nonresonant background.

5. Conclusion

We have investigated a fundamental aspect of image formation in parametric nonlinear optical microscopy, specifically CARS, using a combined numerical-experimental approach. In fluorescence microscopies, the spatial distribution of emitting molecules is directly mapped onto image intensity: this is not so for parametric nonlinear optical detection. We considered CARS imaging of a single Raman-active sphere, centered on the laser propagation axis, in the presence of a smooth nonresonant background. We observed experimentally that the TPEF signal is symmetric about the laser focal plane, whereas the CARS signal is both asymmetric and displaced with respect to this plane. In the FDTD calculations, the detected CARS signal pattern is also seen to be asymmetric about the focal plane. Furthermore, when the sphere is located before the focal plane, there is a distinct ‘shadow’ in the detected signal and this is also observed experimentally. The maximum signal is detected when the scatterer is located behind the laser focal plane. Through an analytical model, we confirmed that the ‘shadow’ results from interference between the nonresonant and resonant CARS signals, and that this asymmetry is caused by the Gouy phase shift. In our future studies, we will investigate other processes affecting image formation in nonlinear microscopy. We anticipate that this general numerical approach to the nonlinear microscopy of spatially highly heterogeneous samples, of which live cells are a prominent example, will play an important role in furthering the utility and applicability of coherent Raman microscopies.

A. A Phenomenological Model of Interference Between the Resonant and Nonresonant Signals

Here we present a derivation of Eq. (4), using the Green function formalism of Ref. [9]. We assume that both the pump and Stokes laser beams can be described by a linearly polarized Gaussian beam of width w_0 and Rayleigh length x_R :

$$\begin{aligned}
 E_{x_{p,s}}(x, r) &= 0, \\
 E_{y_{p,s}}(x, r) &= \frac{E_{0p,s}}{\sqrt{1 + (x/x_R)^2}} \exp\left(-\frac{r^2}{w_0^2(1 + (x/x_R)^2)} + i(k_{p,s}x - \omega_{p,s}t + \phi_G(x, r) + \phi_0)\right), \\
 E_{z_{p,s}}(x, r) &= 0, \\
 \phi_G(x, r) &= -\arctan(x/x_R) + \frac{xr^2}{x_R w_0^2(1 + (x/x_R)^2)},
 \end{aligned} \tag{8}$$

where indices p and s correspond to pump and Stokes, respectively, E_0 is the field amplitude, ϕ_0 an arbitrary phase, and \hat{x} is the direction of the laser propagation; $x = 0$ corresponds to the position of the laser focus. We also assume that the following condition is fulfilled everywhere in space (cf. [9])

$$k_{as} = 2k_p - k_s = (2\omega_p - \omega_s)n/c, \tag{9}$$

where k is the wave vector length, as stands for the anti-Stokes signal, n is the constant linear refraction index in the medium and c speed of light. Eq. (9) is a reasonable approximation for tightly focused lasers.

Let us discuss the nonresonant signal first. Consider a point A located at position (x, r) . Interaction between the nonresonant medium and the pump and Stokes beams gives rise to the nonlinear polarization excited at the anti-Stokes frequency at point A . Assuming an isotropic medium with weak nonlinearity and thus no coupling between different frequencies, this polarization is

$$\begin{aligned}
 P_{x_{asNR}}^{(3)}(x, r) &= 0, \\
 P_{y_{asNR}}^{(3)}(x, r) &= \chi_{NR}^{(3)} E_{y_p}^2(x, r) E_{y_s}^*(x, r) = \\
 &= \frac{\chi_{NR}^{(3)} E_{0p}^2 E_{0s}}{[1 + (x/x_R)^2]^{3/2}} \exp\left(-\frac{3r^2}{w_0^2(1 + (x/x_R)^2)}\right) e^{i(k_{as}x - \omega_{as}t + \phi_G(x, r) + \phi_0)}, \\
 P_{z_{asNR}}^{(3)}(x, r) &= 0,
 \end{aligned} \tag{10}$$

where $\chi_{NR}^{(3)}$ is the (purely real) third-order susceptibility of the medium. Substituting $\vec{P}_{yNR}^{(3)}(x, r)$ into Eq. (13) of Ref. [9], one can write the nonresonant anti-Stokes signal at a point $P = (x_P, 0)$

located on the laser axis in the far-field zone (*i.e.*, $x_P \gg x_R$)

$$\begin{aligned}
E_{x_{as}NR}(P) &= 0, \\
E_{y_{as}NR}(P) &= -\frac{\omega_{as}^2}{c^2} \frac{\exp(ik_{as}x_P)}{x_P} \int_{-\infty}^{\infty} dx \int_0^{\infty} 2\pi r dr \exp(-k_{as}x) P_{y_{as}NR}^{(3)}(x, r) = \\
&\quad -\frac{\omega_{as}^2}{c^2} \frac{\exp(i(k_{as}x_P - \omega_{as}t + \phi_0))}{x_P} \int_{-\infty}^{\infty} dx \int_0^{\infty} 2\pi r dr \times \\
&\quad \frac{\chi_{NR}^{(3)} E_{0p}^2 E_{0s}}{[1 + (x/x_R)^2]^{3/2}} \exp\left(-\frac{3r^2}{w_0^2(1 + (x/x_R)^2)}\right) e^{i\phi_G(x, r)} = \\
&\quad -\frac{\omega_{as}^2}{c^2} \frac{\exp(i(k_{as}x_P - \omega_{as}t + \phi_0))}{x_P} \frac{w_0^2 x_R \pi^2}{2} \chi_{NR}^{(3)} E_{0p}^2 E_{0s}, \\
E_{z_{as}NR}(P) &= 0,
\end{aligned} \tag{11}$$

or

$$E_{y_{as}NR}(P) = -E_{0NR} \exp(i(k_{as}x_P - \omega_{as}t + \phi_0)), \tag{12}$$

where E_{0NR} is the overall amplitude of the nonresonant signal.

We now discuss the response of the resonant spherical scatterer of radius R located on the laser axis at point $(x_0, 0)$. The resonant nonlinear susceptibility at the anti-Stokes frequency is purely imaginary; we denote it as $i\chi_R^{(3)}$, where $\chi_R^{(3)}$ is a positive real number. If $R \ll w_0, x_R$ then the nonzero component of the nonlinear polarization is

$$P_{y_{as}R}^{(3)}(x, r) = \begin{cases} \frac{i\chi_R^{(3)} E_{0p}^2 E_{0s}}{[1 + (x_0/x_R)^2]^{3/2}} e^{i(k_{as}x - \omega_{as}t + \phi_G(x_0, 0) + \phi_0)}, & \text{if } (x - x_0)^2 + r^2 \leq R^2 \\ 0, & \text{otherwise.} \end{cases} \tag{13}$$

Substituting Eq. (13) into Eq. (13) of Ref. [9] and performing the spatial integration, we obtain the resonant signal at the point P

$$\begin{aligned}
E_{y_{as}R}(P) &= -\frac{\omega_{as}^2}{c^2} \frac{\exp(ik_{as}x_P)}{x_P} \int_{-\infty}^{\infty} dx \int_0^{\infty} 2\pi r dr \exp(-k_{as}x) P_{y_{as}R}^{(3)}(x, r) = \\
&\quad -\frac{\omega_{as}^2}{c^2} \frac{\exp(i(k_{as}x_P - \omega_{as}t + \phi_G(x_0, 0) + \phi_0 + \frac{\pi}{2}))}{x_P} \frac{4\pi}{3} R^3 \frac{\chi_R^{(3)} E_{0p}^2 E_{0s}}{[1 + (x_0/x_R)^2]^{3/2}},
\end{aligned} \tag{14}$$

or

$$E_{y_{as}R}(P) = -\frac{E_{0R}}{[1 + (x_0/x_R)^2]^{3/2}} \exp(i(k_{as}x_P - \omega_{as}t + \phi_G(x_0, 0) + \phi_0 + \frac{\pi}{2})), \tag{15}$$

where E_{0R} is the amplitude of the resonant signal, generated by the scatterer located at the origin.

If the linear index mismatch is nonzero, this can result in both amplitude and phase of the resonant signal being changed. For a small scatterer, however, these changes will be small. For this qualitative model, we neglect the change in amplitude of the signal, but will keep the phase shift, since even small phase shifts in the resonant signal can noticeably affect the interference with the nonresonant signal. The resonant signal is then

$$E_{y_{\omega_{as}R}}(P) = -\frac{E_{0R}}{[1 + (x_0/x_R)^2]^{3/2}} \exp(i(k_{as}x_P - \omega_{as}t + \phi_G(x_0, 0) + \phi_0 + \frac{\pi}{2} + \delta\phi_L)), \tag{16}$$

where $\delta\phi_L$ is the phase shift resulting from the linear index mismatch.

Absorbing the negative sign in Eqs. (12) and (15) into the arbitrary phase ϕ_0 and taking the real part, one readily obtains Eq. (4).

Acknowledgments

We would like to acknowledge fruitful discussions with M. Spanner. This work was supported by the Natural Sciences and Engineering Research Council of Canada, Ontario Ministry of Research and Innovation, Canada Research Chairs program, Canada Foundation for Innovation and MITACS NCE Postdoctoral Research Program.